Broadband coherent anti-Stokes Raman scattering for crystalline materials

Franz Hempel,[1,*,†] Sven Reitzig,[1,*,‡] Michael Rüsing,[1] and Lukas M. Eng[1,2]
[1]*Institut für Angewandte Physik, Technische Universität Dresden, 01062 Dresden, Germany*
[2]*ct.qmat: Dresden-Würzburg Cluster of Excellence–EXC 2147, TU Dresden, 01062 Dresden, Germany*

(Received 5 October 2021; accepted 9 December 2021; published 30 December 2021)

Broadband coherent anti-Stokes Raman scattering (B-CARS) has emerged in recent years as a promising chemosensitive high-speed imaging technique. B-CARS allows for the detection of vibrational sample properties in analogy to spontaneous Raman spectroscopy, but also makes electronic sample environments accessible due to its resonant excitation mechanism. Nevertheless, this technique has only gained interest in the biomedical field so far, whereas CARS investigations on solid-state materials are rare and concentrate on layered, two-dimensional materials such as graphene and hexagonal boron nitride . In this work, we discuss the specific properties of this technique when applied to single-crystalline samples, with respect to signal generation, phase matching, and selection rules in the model systems lithium niobate and lithium tantalate. Via polarized B-CARS measurements and subsequent phase retrieval, we validate the predicted selection rules, unequivocally assign the phonons of the A_1(TO), E(TO) and A_1(LO) branches to the detected CARS peaks, and address differences in spontaneous Raman spectroscopy concerning peak frequencies and scattering efficiencies. We thus establish this technique for future investigations of solid-state materials, specifically in the field of ferroelectric single crystals.

DOI: 10.1103/PhysRevB.104.224308

I. MOTIVATION

Microscopical spectroscopy techniques are of fundamental importance for scientific fields ranging from biology to crystallography and material sciences due to their cost efficiency, ease of use, and versatile detection options with spatial resolutions down to the diffraction limit. One of these techniques, coherent anti-Stokes Raman scattering (CARS), has seen increased use for chemosensitive imaging in recent years. CARS is a coherent four-wave mixing (4WM) Raman-scattering technique that resonantly enhances anti-Stokes scattering processes. The third-order nonlinear CARS process is described by a $\chi^{(3)}$ tensor. Owing to its coherent nature and spectral sensitivity, it enables chemically and structurally sensitive investigations with high signal intensities. Due to these features, CARS has gained attention primarily for imaging of biological structures [1–3]. In the field of solid-state materials, however, CARS has only been used for the analysis of low-dimensional materials like carbon nanotubes (CNTs) [4,5], graphene [6–8], and hexagonal boron nitride (hBN) [9]. So far, no investigations of bulk single crystals have been reported, to the best of our knowledge.

Compared with typical biological samples or two-dimensional (2D) materials, CARS investigations within solid, single-crystalline materials come with additional challenges. For example, inorganic crystals usually exhibit much higher absolute refractive indexes n, as well as a larger dispersion than the aqueous media of biological tissue [e.g., $n_{\mathrm{SiC}}(1064\ \mathrm{nm}) = 2.59$, $n_{\mathrm{GaAs}}(1064\ \mathrm{nm}) = 3.45$, whereas $n_{\mathrm{H_2O}}(1064\ \mathrm{nm}) = 1.32$). This significantly impacts the phase matching between interacting waves and causes a stronger distortion of the incident laser beams and of the respective focal point. Furthermore, in anisotropic crystals, birefringence might additionally disturb the focal overlap of the lasers, hence causing additional complexity in phase matching. Moreover, in bulk crystals the nonlinear material usually fills the complete focus area, while biological cell structures are usually only several hundred nanometers to a micron in thickness. Thus, phase matching considerations become much more relevant to bulk crystals [10]. Solid-state samples also may show large electronic backgrounds that might additionally disturb the resonant vibrational CARS signal. Finally, the vibrational motions detected in crystals are not molecular vibrations without directional orientation but phonons that possess an inherent momentum q. While for idealized crystals it may be assumed that only phonons with zero momentum ($q = 0$) are detected, defects in real crystals cause the detection of phonons with $q \neq 0$. These defects in crystal structures thus provide an additional complexity in the analysis of CARS data.

In contrast with these challenges, the CARS technique exhibits distinct advantages in comparison to the established technique of spontaneous Raman scattering (SR). Similar to SR, the CARS process is sensitive to vibrational motions. However, the $\chi^{(3)}$ tensors that determine the CARS efficiency obey different selection rules, providing advantages for certain scenarios [11], and enable a higher sensitivity to geometry changes in the scattering process when compared with SR [12]. Furthermore, whereas SR shows a comparably low scattering efficiency and thus requires long acquisition times in regard to hyperspectral imaging, the nonlinear nature of CARS allows a much faster spectral acquisition, especially

---

[*] These authors contributed equally to this paper.

[†] franz.hempel@tu-dresden.de

[‡] sven.reitzig@tu-dresden.de

when implementing broadband CARS (B-CARS), where a broadband laser source is used to detect the full CARS spectrum at once. Additionally, the signal generation only takes place under tight focusing, while the SR signal is generated into the full depth of the illuminated volume. Therefore, CARS allows for depth-sensitive imaging without the need for a confocal pinhole, as is necessary in SR. These features make CARS an ideal technique for fast imaging of structural features in crystals, such as strain fields, local stoichiometry variations, or changes in the crystal structure.

For these reasons, we present a fundamental case study of B-CARS investigations on selected single crystals. As model systems, we investigate lithium niobate (LN) and lithium tantalate (LT) that are both ferroelectric crystals of the C_{3v} point group. These materials are widely used, especially in integrated optics, electro-optic modulators, or in nonlinear optics [13–19] because their crystal structure can easily be manipulated to create ferroelectric domains. Furthermore, the development of conducting domain walls makes them also promising for reconfigurable electronic setups [20,21]. They thus are materials of high interest for the scientific community and well suited to serve as model materials.

In this work, we experimentally evaluate the influence of the above-listed challenges to provide a fundamental contribution to the investigation of solid-state properties via CARS. We address basic assumptions about phase matching of the mixed waves and extract the resonant response of recorded CARS spectra via phase retrieval algorithms that have been developed for the spectral error correction of CARS spectra on biological samples [22]. By comparison with reported SR peak frequencies, the peaks of error-corrected resonant anti-Stokes spectra are assigned where possible, and the validity of the selection rules that are calculated from reported $\chi^{(3)}$ tensors [11] is examined.

This work thus lays the foundation for future B-CARS investigations of single crystalline materials in solid-state physics.

II. THE CARS PROCESS

A. Theory of B-CARS signal generation

CARS is a coherent technique of Raman scattering. Other than SR, which is based on the inelastic scattering of single photons on the analyte, the CARS mechanism requires the coherent interaction of three incident laser photons with spatial, temporal, and phase overlap to generate a resonantly enhanced anti-Stokes shift. The energy schemes of SR (with either Stokes or anti-Stokes scattering) are shown in the Jablonski diagrams in Figs. 1(a) and 1(b). In spontaneous Stokes scattering, a sample's energy level is excited to a virtual state by the incident photon and returns to an excited vibrational state Ω by emitting a photon with a lower energy than the incident photon. In contrast with that, the sample is already excited to a higher vibrational state in (incoherent) spontaneous anti-Stokes scattering (SAS), e.g., by thermal energy. Upon further excitation to the virtual state via the incident photon, it returns to the vibrational ground state E, thus emitting a photon with a higher energy than the incident photon.

For the CARS process, a pump pulse ω_{pu} and a Stokes pulse ω_s interact coherently to increase a material's vibrational level by an energy amount equivalent to their difference frequency $\Delta\omega = \omega_{pu} - \omega_s$. If $\Delta\omega$ fits the energy difference between the material's vibrational ground state and a real excited state, the excited vibrational state then is resonantly populated. A probe pulse ω_{pr} may then induce anti-Stokes scattering so that the detected anti-Stokes pulse has an energy of $\omega_{as} = \omega_{pu} - \omega_s + \omega_{pr}$. In CARS setups with monochromatic Stokes lasers, it is necessary to tune the Stokes laser wavelength in order to record a full CARS spectrum. In B-CARS, however, a broadband Stokes laser is applied to record a full spectrum simultaneously, thus allowing for a fast spectral acquisition. The Jablonski diagram in Fig. 1(c) shows the specific mechanism of B-CARS. In most cases, the probe pulse is generated by the same laser as the pump pulse ($\omega_{pu} = \omega_{pr}$).

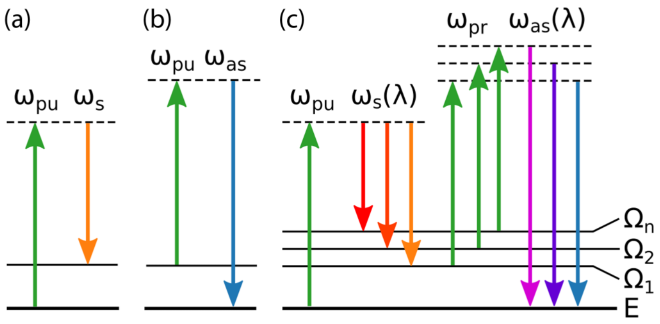

FIG. 1. Jablonski diagrams of (a) spontaneous Stokes scattering, (b) spontaneous anti-Stokes scattering, and (c) B-CARS.

Due to the 4WM signal-generation process, CARS exhibits a signal with a third-order nonlinearity. A sample's CARS response is described by the third-order nonlinear susceptibility $\chi^{(3)}(\omega)$ [23]. Furthermore, the detected signal is also influenced by the optical properties of the setup, e.g., transmission values of the applied microscope objective. These specific setup properties can be mathematically described as an effective stimulation profile $\tilde{C}(\omega)$. The CARS signal thus shows the following proportionality [22]:

$$I_{\text{CARS}}(\omega) \propto |\tilde{C}(\omega)|^2 |\chi^{(3)}(\omega)|^2. \tag{1}$$

In CARS, the nature of the signal is determined by the energy difference between the pump and Stokes laser. Whereas the CARS signal is resonantly enhanced for the occupation of real vibrational energy levels (i.e., phonons or molecular vibrations), electronic contributions to the 4WM process generate a nonresonant background (NRB) for each combination of pump and Stokes laser energies [11]. The nonlinear susceptibility tensor therefore is the sum of a resonant part $\chi_R^{(3)}$ and a nonresonant part $\chi_{\text{NRB}}^{(3)}$:

$$\chi^{(3)} = \chi_R^{(3)} + \chi_{\text{NRB}}^{(3)}. \tag{2}$$

The combination of Eqs. (1) and (2) yields the calculated CARS signal as follows:

$$I_{\text{CARS}} \propto |\tilde{C}(\omega)|^2 \left(\left|\chi_R^{(3)}\right|^2 + \left|\chi_R^{(3)} \chi_{\text{NRB}}^{(3)}\right| + \left|\chi_{\text{NRB}}^{(3)}\right|^2 \right). \tag{3}$$

For the comparison of CARS spectral data with SR, only the resonant part $\chi_R^{(3)}$ should be considered. While the pure NRB term $|\chi_{\text{NRB}}^{(3)}|^2$ acts only as an additive underground signal, the resonant-nonresonant mixed term $|\chi_R^{(3)}\chi_{\mathrm{NRB}}^{(3)}|$ distorts peak shapes and obscures peak positions and widths in raw B-CARS spectra. To be able to compare such CARS data with SR, it is necessary to correct for the influence of the NRB.

B. Extraction of spectral information

To extract the SR-like information from the raw CARS data, the influence of the NRB needs to be corrected. Experimentally, this can be realized via angular-resolved measurements of anisotropic vibrational modes [24] or time-resolved detection [25] because the resonant CARS signal is generated with a time delay with respect to the NRB due to the occupation of real vibrational states. In a mathematical approach, the resonant signal can be isolated via phase retrieval (PR) algorithms in postproduction. These are based on the assumption that, while $\chi_R^{(3)}$ is a complex value with real and imaginary parts, $\chi_{\mathrm{NRB}}^{(3)}$ is a purely real value since the NRB contribution is energetically far from any electronic resonance [22]. The imaginary part of the resonant response $\mathrm{Im}\{\chi^{(3)}\}$ is approximated to be proportional to the signal of SR [26]. This allows us to directly compare the obtained CARS data with SR via extraction of the imaginary part of the resonant signal. Extraction is realized via either the maximum entropy method [27] or by using a modified Kramers-Kronig transform (KK) [22].

In this work, we apply the Python package CRIKIT2 by Camp *et al.* [22], which utilizes a KK-based PR routine. In short, CRIKIT2 applies the Hilbert transform $\hat{\mathcal{H}}$, a special case of the Kramers-Kronig relation that describes the relation between the absolute value and the complex phase ϕ of a given signal $f(\omega)$:

$$\ln|f(\omega)| = -\hat{\mathcal{H}}\{\phi(\omega)\}, \tag{4}$$

$$\hat{\mathcal{H}}\{f(x)\} = \frac{\mathcal{P}}{\pi}\int \frac{f(x')}{x-x'}\partial x'. \tag{5}$$

$\mathcal{P}$ denotes the Cauchy principal value. Because the measured signal is spectrally limited, the windowed Hilbert transform $\hat{\mathcal{H}}_W$ for limited signals is used. The peak distortion shown in Eq. (3) is corrected by applying the Hilbert transform to $I_{\mathrm{CARS}}/I_{\mathrm{NRB}}$ because the phase contribution of the nonresonant real part is zero:

$$\phi_{\mathrm{CARS/NRB}}(\omega) = \hat{\mathcal{H}}_W\left\{\frac{1}{2}\ln\frac{I_{\mathrm{CARS}}(\omega)}{I_{\mathrm{NRB}}(\omega)}\right\}. \tag{6}$$

The PR spectrum $I_{PR}(\omega)$ is calculated as follows:

$$I_{PR}(\omega) = \sqrt{\frac{I_{\mathrm{CARS}}(\omega)}{I_{\mathrm{NRB}}(\omega)}}\exp\left[i\phi_{\mathrm{CARS/NRB}}(\omega)\right]. \tag{7}$$

For biological imaging where this technique has been established, the NRB spectrum would typically be extracted from a pixel of the mapped area where no organic matter is present. Because we are measuring bulk crystals, this procedure is not applicable. Thus, the NRB spectrum was acquired by a separate measurement on an empty glass slide because glass does not show distinct Raman modes or other $\chi^{(3)}$ resonances in the spectral range of interest. Typically, the spectrum of the NRB reference measurement also differs from the (not experimentally available) pure NRB signal of the analyte. The error correction algorithms of CRIKIT2 account for these resulting transformation errors caused by the inaccurate NRB. Because this correction eliminates the detector function $\tilde{C}(\omega)$ as well, we thus obtain spectra that can be quantitatively compared with error-corrected data from other CARS setups.

C. Phase-matching calculations

Like any other nonlinear optical process, the CARS 4WM process requires not only a spatial and temporal overlap of the pump-probe and Stokes laser beam but also phase matching of the interacting lasers (pump and probe, Stokes and anti-Stokes signal) to reach high conversion efficiencies. However, the dispersion of the refractive index in dependence on the laser wavelengths leads to a phase mismatch that limits the effective volume of signal generation. The CARS signal is generated under tight focusing conditions within the depth of focus. Given the pump-laser wavelength of 1064 nm and a water-dipping microscope objective with a NA of 0.8, the depth of focus can be approximated as 2.2 μm at the sample surface and 3.8 μm with the focus placed deeply within a LN sample (ordinary axis). However, if the nonlinear coherent interaction length l_c—that is, the length over which constructive interference of the involved lasers is maintained before phase mismatch leads to destructive interference—is lower than the depth of focus, the generated signal will be decreased. The proportionality between l_c and the generated CARS signal intensity I_{CARS} is [28]

$$I_{\mathrm{CARS}} \propto l_c^2. \tag{8}$$

In analogy to phase matching considerations in SH microscopy [29], l_c can be calculated via the k-vector mismatch Δk in dependence on wavelengths λ and respective refractive indexes n at the wavelengths of the involved lasers in the analyte crystal with

$$l_c = 2\pi/|\Delta k|, \tag{9}$$

$$\Delta\vec{k} = \vec{k}_{pu} - \vec{k}_s + \vec{k}_{pr} \pm \vec{k}_{as}, \tag{10}$$

$$|k| = \frac{2\pi n}{\lambda}. \tag{11}$$

Equation (10) is derived from the B-CARS scheme (Fig. 1) for a collinear setup, i.e., the incident photons all propagate along the same direction. Depending on the direction in which the anti-Stokes signal is generated, the term k_{as} is either added (for counterpropagation or backscattering) or subtracted (for copropagation or forward scattering). In our setup, pump and probe photons are generated from the same laser source, so the equation can be simplified with $k_{\mathrm{pr}} = k_{\mathrm{pu}}$. With these considerations, l_c is calculated for both co- and counterpropagation of the signal via

$$l_{c,\,\mathrm{co}} = \frac{1}{2\left(\frac{2n_{pu}}{\lambda_{pu}} - \frac{n_s}{\lambda_s} - \frac{n_{as}}{\lambda_{as}}\right)}, \tag{12}$$

$$l_{c,\,\mathrm{counter}} = \frac{1}{2\left(\frac{2n_{pu}}{\lambda_{pu}} - \frac{n_s}{\lambda_s} + \frac{n_{as}}{\lambda_{as}}\right)}. \tag{13}$$

Following these equations, l_c depends on the specific laser wavelengths and refractive indexes involved. This means that, for each anti-Stokes shift of the CARS spectrum, the phase-matching conditions must be specifically calculated. For anisotropic media, the polarization direction of incident and detected photons must be considered as well because the change of refractive indexes affects l_c. However, independent of the specific laser polarizations and spectral positions, we observe that in LN and LT, l_c is always several orders of magnitude larger for copropagation than for counterpropagation. Naturally, the generated forward-scattered CARS signal must also be several orders of magnitude larger than the backscattered CARS signal. As an example, the phase-matching conditions on z-cut LN (polarization of the incoming and generated waves along the ordinary axes) for a signal at $-867\ \text{cm}^{-1}$ are

$$l_{\text{c, co}}(-867~\text{cm}^{-1}, \text{ordinary}) = 0.42\ \text{m}, \tag{14}$$

$$l_{\text{c, counter}}(-867~\text{cm}^{-1}, \text{ordinary}) = 109 \times 10^{-9}\ \text{m}. \tag{15}$$

With the results of Eqs. (14) and (15) and the relation (8), it can be concluded that the magnitude of the CARS signal is almost exclusively generated in the forward-scattering direction, similar to observations made for second-harmonic generation microscopy [29]. The relevance of these considerations for CARS measurements on crystals when using a backscattering setup will be experimentally evaluated later in this work.

D. CARS selection rules

For the analysis of the PR B-CARS spectra and the respective phonon assignment for LN and LT, it is crucial to predict the selection rules of 4WM processes in crystals of the C_{3v} point group. As a basis for these predictions, we used reported CARS tensors from the literature [11]. In analogy with SR, only the signals connected to A_1 or E phonons can be detected with 4WM processes. The generated CARS responses for A_1 and E phonons and their respective polarizations can be predicted by calculating the dot product of the $\chi^{(3)}$ vector and the unit vector $\vec{e}$ of the incident photons for all electric-field polarization combinations (relative to the crystal axes) of pump, probe, and Stokes laser. Based on these predictions, a selection-rule table for all collinear CARS geometries with $\vec{e}_{pu} = \vec{e}_{pr}$ was created, in accordance with the specifications of our setup. For the indication of the CARS geometry, an extended Porto notation is used here, following the structure of Eq. (16),

$$\vec{k}_{pu,pr,s}(\vec{e}_{pu}\vec{e}_{pr}\vec{e}_s, \vec{e}_{as})\vec{k}_{as}, \tag{16}$$

where $\vec{k}$ is the k vector, $\vec{e}$ is the unit vector, pu is the pump laser, pr is the probe laser, s is the Stokes laser, and as is the anti-Stokes signal.

As an example, in the CARS geometry $z(xxy, y)$-z the incident lasers propagate along the z axis of the crystal, pump and probe lasers are polarized along the x axis, and the Stokes laser is polarized along the y axis. The anti-Stokes signal is then detected in backscattering along the z axis with a polarization along the y axis of the crystal.

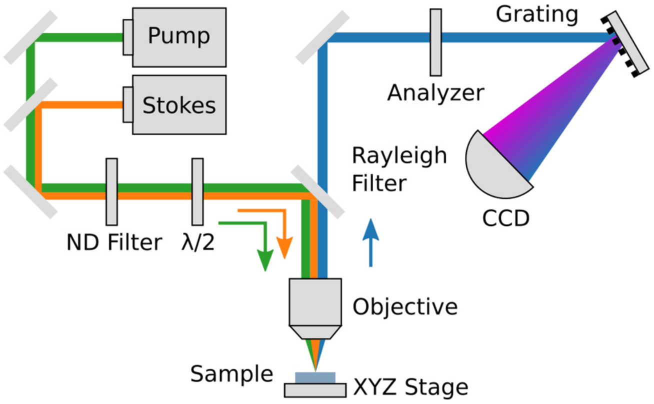

FIG. 2. B-CARS setup applied in this work. The pulsed incident pump (1064 nm) and broadband Stokes laser (600–2000 nm) are matched spatially, temporally, and in phase. Measurements are conducted in the backscattering geometry. ND: neutral density filter, λ/2: rotatable half-wave plate, CCD: charge-coupled device.

Following the predicted selection rules, we can specifically address the CARS geometries that allow for detecting the different phonon branches of LN and LT. Complete selection rule tables for all collinear backscattering geometries with $\vec{e}_{pu} = \vec{e}_{pr}$ are provided in Tables S1–S3 of the Supplemental Material [30].

III. CARS MEASUREMENT PROCEDURE

To explain the experimental procedure and data analysis process carried out here, we describe our setup and demonstrate the phase retrieval based on a spectrum of z-cut congruent LN (cLN) in this section. We further experimentally investigate the fundamental influence of CARS properties, such as the nonlinearity of the CARS signal intensity and phase matching, and consider influence factors that are specific to Raman investigations on crystals, such as the numerical aperture (NA) of the microscope objective and the stoichiometry of the sample.

A. Setup

The B-CARS and comparative SR measurements were conducted on a LabRAM HR Evolution commercial Raman microscope (HORIBA Jobin Yvon GmbH, Oberursel, Germany). The measurements were done in backscattering geometry with a Nikon CFI APO NIR 40× water-dipping objective (NA = 0.8). A sketch of the B-CARS setup is shown in Fig. 2.

The incident pump and probe and Stokes pulses are generated by a combined laser system (LEUKOS CARS-SM-30) and are matched temporally, spatially, and in phase. The monochromatic pump-probe laser has a central wavelength of 1064 nm and the broadband Stokes laser emits in the wavelength range of 600–2000 nm. A high-pass filter eliminates the Stokes laser signal below 1064 nm to avoid interference with the anti-Stokes signal. For comparative SR measurements, a 632.8 nm monochromatic He-Ne continuous-wave laser (Melles Griot) is used. The polarization of the incoming and

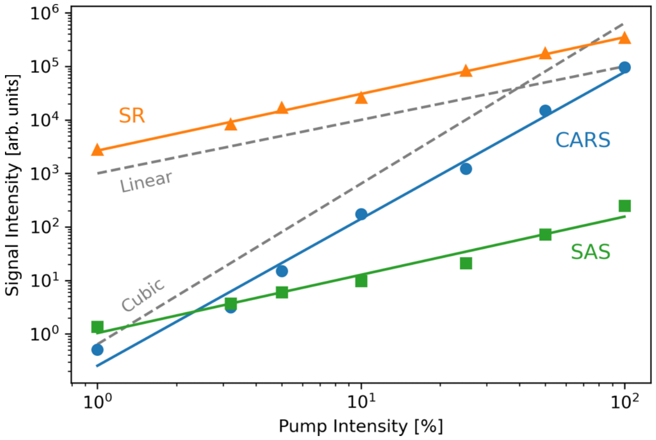

FIG. 3. Detected signal intensities of SR (orange triangles), SAS (green squares), and raw B-CARS (blue dots) depending on incident laser intensities (in percent relative to the nominal laser power). The slopes for linear and cubic relations are given in black as a guide to the eye (dashed lines).

detected signal are controlled by a rotatable half-wave plate and a rotatable linear polarization filter (Glan-Taylor prism), respectively. Our detector setup provides a spectral resolution of 0.05 nm (0.45–0.56 cm^{-1} over the full spectral range) for the CARS measurements and 0.013 nm (0.28–0.33 cm^{-1}) for SR. Additional setup parameters are provided in the Supplemental Material [30].

B. Samples

For this case study, we investigated single-crystalline wafers of undoped congruent LN and LT (x, y, and z cut) by Impex HighTech GmbH (subsequently referred to as cLN and cLT). The wafers exhibit a surface roughness of $R = 0.25$nm and a thickness of $t = 500 \pm 25$ μm.

C. Nonlinearity

To verify that the signal in our B-CARS measurements results from a 4WM process, the nonlinearity of the detected signal intensity was examined via measurements at varying laser intensities. For these measurements, we monitored the SR, the raw B-CARS, and the spontaneous anti-Stokes (SAS) response on the CARS pump laser (1064 nm). The integrated signal intensities of the 860 cm^{-1} peak in SR, SAS, and raw B-CARS spectra are plotted against the relative pump intensities (in percent relative to the nominal laser powers) in Fig. 3.

The double-logarithmic plot allows for easy determination of the proportionality exponent $I_{\mathrm{CARS}}, I_{\mathrm{SR}}, I_{\mathrm{SAS}} \propto I^{\alpha}_{\mathrm{Pump}}$ from the slope of the data. As seen, the SR and SAS signals both exhibit the expected linear relation between incident laser power and detected signal because both the spontaneous Stokes and anti-Stokes scattering mechanisms are two-wave mixing processes with one incident and one emitted photon each. The measured B-CARS peak intensities verify the nonlinear characteristics with an exponent of $\alpha = 2.74 \pm 0.13$. Nevertheless, this is less than the expected cubic relation $I_{as} \propto I_p^2 I_{pr}$, which might be caused by losses either in the optical path of the setup or in the sample itself.

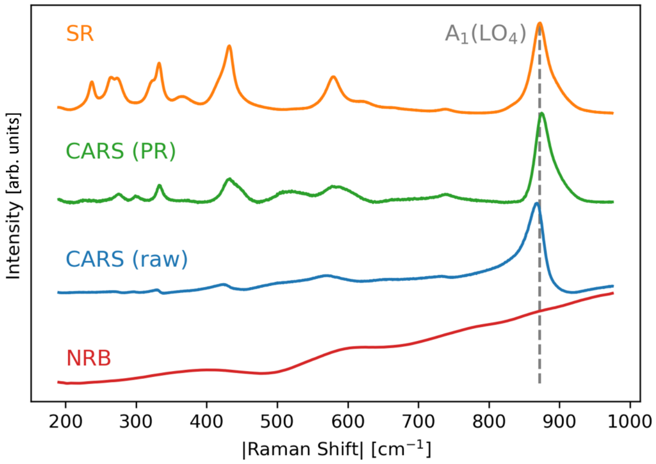

FIG. 4. Phase retrieval of a raw B-CARS spectrum of z-cut cLN via NRB measurement and comparison with SR data. From bottom to top: NRB spectrum (red) measured with B-CARS on a microscope glass slide, raw B-CARS spectrum (blue), phase-retrieved B-CARS spectrum (green), SR spectrum (red) for the respective sample geometry. Spectra are plotted over the modulus of the Raman shift to provide a direct comparison of B-CARS data with SR data.

D. Example of phase-retrieval procedure

To demonstrate the process of phase retrieval on the detected B-CARS spectra, the raw and PR spectra of cLN in the system geometry $z(xxx, x)\text{-}z$ (extended Porto notation) and the NRB spectrum applied for PR are depicted in Fig. 4 and compared with the respective SR spectrum. Please note, in opposition to Stokes shifts, the anti-Stokes shifts that are detected in CARS are defined as negative values. However, to directly compare the B-CARS spectra with the positive values of SR, we refer here to the modulus of the CARS anti-Stokes shifts.

The raw B-CARS spectrum exhibits one dominating peak at 860 cm^{-1} that shows a distinct asymmetry at the base and is shifted towards a lower frequency as compared with the peak position in SR (870 cm^{-1}). Other peaks at lower frequencies are covered by the NRB signal and are therefore difficult to analyze. The NRB spectrum was taken on a microscope glass slide because glass does not exhibit distinct Raman peaks that could be resonantly enhanced. As stated earlier, the separate NRB measurement on a nonresonant sample yields a different NRB background than the one that is active in the actual measurement on cLN. However, the applied error-correction algorithm is able to correct for inaccurate NRB spectra as well. After phase retrieval, the peaks are remarkably more symmetrical (i.e., “Raman-like”) and the peak positions are notably closer to those in SR. Additionally, the peaks in the lower spectral range become visible now and in general match the peaks in the comparative SR spectrum. The SR spectrum was taken with the 632.8 nm laser positioned at the same sample spot. A comparison of peaks in the error-corrected spectra with the respective SR data and an unequivocal phonon assignment will be conducted in a section below.

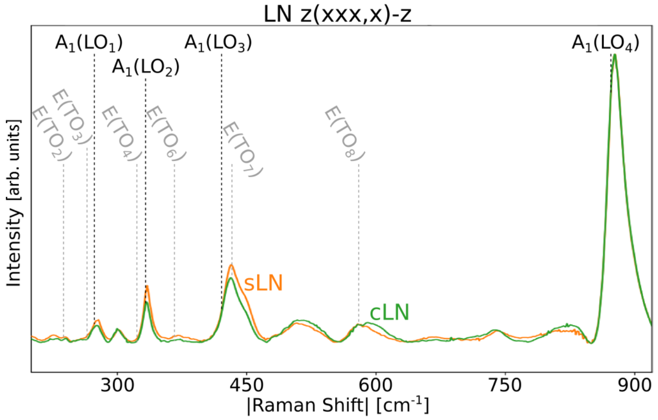

FIG. 5. Phase-retrieved CARS spectra of cLN and sLN in $z(xxx, x)$-z CARS geometry with indicated phonon frequencies reported for SR [31]. The differences between the spectra of the two samples that differ in defect density are comparable to the observations by SR.

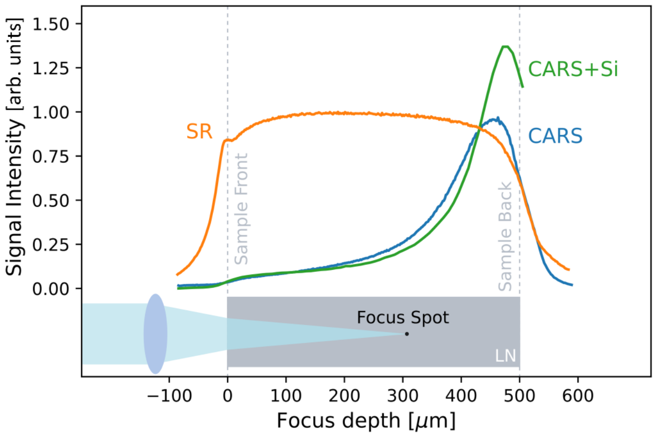

FIG. 6. Depth scan of the CARS intensity on z-cut cLN (thickness = 500 μm) with a free sample backside (blue) and an applied silicon wafer acting as a mirror (green). The detected intensity maximum is close to the sample backside and distinctly increased with a supporting reflective backside. The SR intensity (orange) is shown for comparison.

E. Crystal stoichiometry and numerical aperture

To investigate the influence of defect density in the CARS spectra of cLN, we compared the PR CARS response in $z(xxx, x)$-z for the lithium-deficient congruent LN (cLN) and near-stoichiometric LN (sLN) regarding their spectral features (Fig. 5). Defects in crystal structures, like here induced by the lithium deficiency in cLN, can lead to the detection of phonons with $q \neq 0$, thus causing a broadening of the detected phonon peaks, as well as the occurrence of anharmonic vibrations. As expected due to the lower defect density, the peaks in the sLN spectrum are narrower than for cLN. For peaks that can be assigned to phonon frequencies, the peak positions and intensities experience minor changes that are comparable to the differences between sLN and cLN in SR [31]. Some of the background peaks also show changes in peak intensity and/or frequency, e.g., in the frequency range around 500 cm^{-1}. Further investigation is necessary to clarify whether these unassigned peaks, which are observed in LT and other geometries as well, are affected by the crystal stoichiometry in a conclusive way.

The numerical aperture NA of the applied microscope objective can also influence the detected spectra in all Raman techniques applied to anisotropic solid-state media [32]. The NA affects the geometry of a Raman measurement following the definition $\mathrm{NA} = n \sin\alpha$ (with n being the refractive index of the surrounding medium, α being the aperture angle). This means that, for a high NA, incident and detected laser photons from other geometries than the nominal one will affect the spectral response due to a higher aperture angle. For cLN in $z(xxx, x)z$, we therefore compared the B-CARS response with the NIR microscope objective LMH-50X-1064 by Thor Labs (NA = 0.65) with the Nikon CFI APO NIR 40× water-dipping objective (NA = 0.8) that was used for all other measurements in this work to assess the influence of the numerical aperture on our B-CARS spectra. Although the spectra are normalized, a lower signal-to-noise ratio indicates a decreased signal intensity for a lower NA. Minor differences between the relative peak intensities of the two measurements are apparent, and the two phonon pairs E(TO$_4$), A$_1$(LO$_2$) and A$_1$(LO$_3$), E(TO$_7$) appear to be slightly blueshifted as compared with the larger NA measurement (<3 cm^{-1}). The small frequency changes of selected phonon peaks associated with phonon directional dispersion [32] cannot be resolved sufficiently with the phase-retrieved CARS spectra to draw meaningful conclusions from the detected shifts, but the comparison of the spectra shows no effects that would not be expected from observations in SR. The spectra are provided in the Supplemental Material (Fig. S2) [30].

F. Phase matching

Naively, one would assume that, in the applied backscattering setup, only the counterpropagating, i.e., backscattered, signal can be detected. However, as we showed in our phase-matching calculations, the counterpropagating signal is very weak due to a short nonlinear coherent interaction length. The copropagating CARS signal, by contrast, is several orders of magnitude stronger. In a transparent crystal such as LN or LT, the forward-scattered signal propagates towards the back side of the sample, where the refractive index jump at the interface between the crystal and air causes reflection for a fraction of the light. The back-reflected forward-scattering CARS signal thus enhances the backscattering signal. Because the copropagating signal is so massively stronger than the counterpropagating response, it is assumed that the detected CARS signal in a backscattering setup is still dominated by the forward-scattering signal. To validate this assumption, we conducted depth scans on z-cut LN and monitored the intensity over the focus depth. The 40× water-dipping objective (NA = 0.8) was used in combination with a 50 μm pinhole for SR and without a pinhole for B-CARS because the CARS depth resolution is limited by the overlap of the two spectral foci. In SR, we would observe a uniformly high signal strength over the full depth of the sample, with only small losses due to absorption and scattering at greater depths. The measured CARS intensity graphs (Fig. 6), however, demonstrate that

TABLE I. Main peak frequencies $\Delta\tilde{\nu}_{\text{Peak}}$ detected in B-CARS measurements on cLN, and phonon assignment based on reported phonon frequencies $\Delta\tilde{\nu}_{\text{Phonon}}$ by SR [31]. Uncertain assignments are given in italic.

$\Delta\tilde{\nu}_{\text{Peak}}$ [cm^{-1}]	Assigned phonon	$\Delta\tilde{\nu}_{\text{Phonon}}$ (SR) [cm^{-1}]
−245	$E(TO_2)$	238
−254	$A_1(TO_1)$	253
−276	$A_1(LO_1)$	275
−279	$E(TO_3)$	265
−283	$A_1(TO_2)$	276
−296	*$E(LO_3)$*	*297*
−333	$E(TO_4)$	322
−335	$A_1(LO_2)$	333
−342	$A_1(TO_3)$	333
−375	$E(TO_6)$	370
−430	$A_1(LO_3)$	418
−447	$E(TO_7)$	433
−508		
−545		
−596	$E(TO_8)$	579
−663	*$E(TO_9)$*	*660*
−880	$A_1(LO_4)$	870

TABLE II. Main peak frequencies $\Delta\tilde{\nu}_{\text{Peak}}$ detected in B-CARS measurements on cLT, and phonon assignment based on reported phonon frequencies $\Delta\tilde{\nu}_{\text{Phonon}}$ by SR [31]. Uncertain assignments are given in italic.

$\Delta\tilde{\nu}_{\text{Peak}}$ [cm^{-1}]	Assigned phonon	$\Delta\tilde{\nu}_{\text{Phonon}}$ (SR) [cm^{-1}]
−200	*$A_1(TO_1)$*	*207*
−210	$E(TO_2)$	209
−256	$E(TO_3)$	253
−229		
−257	*$A_1(LO_1)$*	*256*
−262	$A_1(TO_2)$	256
−283	*$E(LO_3)$*	*282*
−357	$A_1(LO_2)$	355
−360	$A_1(TO_3)$	357
−385	$E(TO_6)$	383
−409	$A_1(LO_3)$	405
−465	$E(TO_7)$	464
−520 . . . 575		
−604	$A_1(TO_4)$	598
−662	$E(TO_9)$	659
−753		
−867	$A_1(LO_4)$	865

the detected signal reaches a maximum with the focus point close to the sample backside. Moreover, adding a silicon wafer for enhancing reflection on the sample backside increases the detected B-CARS signal. Both observations support our assumption of forward scattering being the main source of our CARS signal. Based on these findings, we chose a focus depth of 450 μm for the following CARS measurements to maximize the signal output.

IV. RESULTS

A. Polarized B-CARS on lithium niobate

To verify the previously calculated selection rules, CARS measurements were conducted on LN and LT single crystals in three different geometries that are supposed to allow the detection of A_1(TO), A_1(LO), and E(TO) phonons. The frequencies of assigned phonons in the PR CARS spectra are listed in Tables I (LN) and II (LT), together with reported values by SR [31]. The raw and PR CARS spectra together with the respective SR spectra for all backscattering geometries with $\vec{e}_p = \vec{e}_s = \vec{e}_{pr}$ can be found in the Supplemental Material (Figs. S4 and S5) [30].

Figure 7 shows the SR, raw CARS, and PR CARS spectra of LN in the CARS geometries $x(zzz, z)$-x [Fig. 7(a)], $y(xxx, z)$-y [Fig. 7(b)], and $z(xxx, x)$-z [Fig. 7(c)], and the respective SR geometries $x(zz)$-x [Fig. 7(a)], $y(xz)$-y [Fig. 7(b)], and $z(xx)$-z [Fig. 7(c)]. The dashed lines are a guide to the eye at reported SR phonon frequencies experimentally observed in other works [31,33–35]. The display of raw and PR CARS spectra in line with the respective SR spectra in the

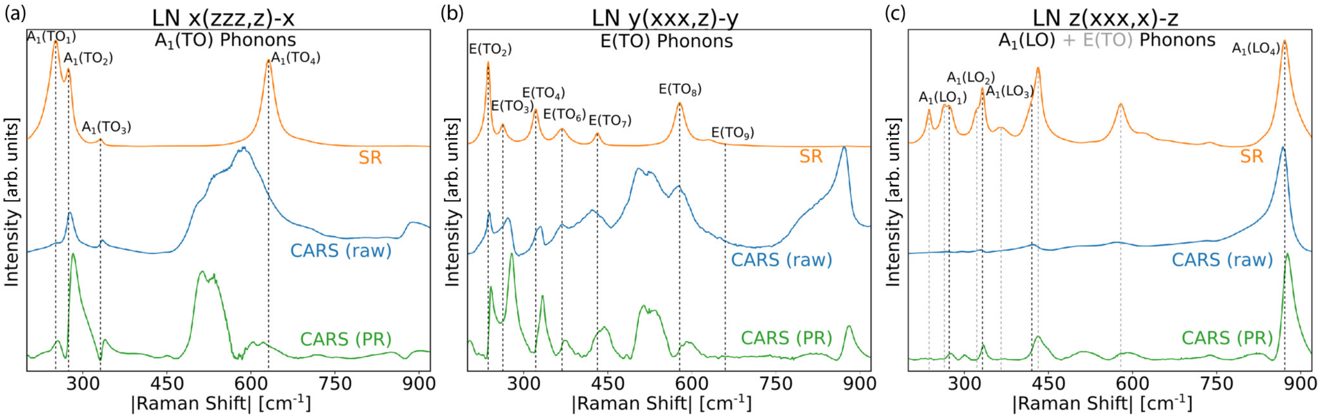

FIG. 7. SR (red), raw CARS (blue), and phase-retrieved (PR) CARS spectra (green) of cLN in (a) $x(zzz, z)$-z, (b) $y(xxx, z)$-y, and (c) $z(xxx, x)$-z geometry. CARS spectra are plotted over the modulus of the Raman shift for comparison with SR data. The A_1(TO), E(TO), and A_1(LO) phonons expected for the respective geometry are indicated by dashed lines that refer to reported values of SR phonon frequencies.

same scattering geometry allows for an intuitive assessment of the phonon assignment and peak frequencies by CARS. In Fig. 7(a), only $A_1(TO)$ phonons are supposed to be detectable in this CARS geometry. The phonons $A_1(TO_1)$ to $A_1(TO_3)$ can be unambiguously assigned. Nevertheless, the peak frequencies of the PR CARS spectrum of LN are shifted to higher values than in SR in all three cases. By comparing the raw and phase-retrieved spectra, it is noticeable that the peaks in the frequency region below $-400\ \mathrm{cm}^{-1}$ are more symmetrical and the peak frequencies of the raw spectrum match the phonon frequencies better than the phase-retrieved signal. Such results are indicative of the strong influence of spontaneous anti-Stokes scattering. In this case, the phase-retrieval scheme distorts the symmetrical peaks and shifts them away from their original frequency. Follow-up experiments that account for the influence of the spontaneous anti-Stokes signal are required to avoid such artifacts. Interestingly, the scattering intensity of $A_1(TO_4)$ in CARS is too low to assign any phonon peak. This is in stark contrast with SR, where the $A_1(TO_4)$ phonon peak exhibits a high peak intensity. The group of peaks between $-500\ \mathrm{cm}^{-1}$ and $-600\ \mathrm{cm}^{-1}$ cannot be assigned to any phonons in LN. Theoretical calculations show that the density of states (DOS) is close to zero in this frequency range [36]. Therefore, the origin of these peaks cannot be an ordinary phonon vibration, neither at the Γ point nor at a different wave vector q in the phonon dispersion of LN [37,38]. There are two possible origins of these unassigned peaks:

(1) The phase retrieval procedure might leave artifacts in the transformation process. This assumption is supported by the fact that these peaks can be found in all measurement geometries, however, with a different magnitude and peak shape in the z-cut spectra (see Fig. S4 in the Supplemental Material [30]). Because the NRB reference spectrum, which was measured on a microscope glass slide, does not show the respective signals like in the LN spectra, these peaks are a material-specific, nonphononic NRB effect rather than a device function. For the same reason, the phase retrieval procedure cannot account for them and thus leaves them unaltered in the phase-retrieved spectra. If it is indeed intrinsic to the LN material system, investigations with other setups should yield the same artifacts. The signal could be manually corrected in the phase-error correction step of the phase retrieval procedure. However, the subtraction of such a large feature would be a significant manipulation of the data and must not be conducted without further knowledge of its origin.

(2) If the detected signals are indeed part of the resonant CARS spectra and not artifacts, possible explanations for these peaks are anharmonic oscillations introduced by crystal defects or an enhanced appearance of two-phonon scattering. In both cases, the CARS selection rules regarded in this paper cannot predict the occurrence of these effects. Further investigations that specifically address such sample properties are necessary to elucidate the origin of these peaks, which cannot be conclusively assigned here. In Fig. 7(b), the applied CARS geometry $y(xxx, z)\text{-}y$ only allows the detection of E(TO) phonons. The comparison with SR data shows that the majority of the peaks from that phonon branch can be detected. However, the assigned peaks of the PR CARS spectrum again exhibit a shift to higher frequencies, similar to Fig. 7(a). The relative intensity ratios of the E(TO) phonon peaks are comparable to those in SR. As an example, the phonon peak of $E(TO_9)$ cannot be assigned in analogy to SR. Again, a group of peaks can be observed at ca. $-500\ \mathrm{cm}^{-1}$, which cannot be assigned to ordinary phonon vibrations. The peak at $-867\ \mathrm{cm}^{-1}$ is either assigned to $A_1(LO_4)$, which is only allowed in z-cut geometries, or to the $E(LO_9)$ phonon that is found at a comparable frequency in SR [$\Delta\tilde{\nu}_{A_1(LO_4)}(SR) = 871\ \mathrm{cm}^{-1}$, $\Delta\tilde{\nu}_{E(LO_9)}(SR) = 878\ \mathrm{cm}^{-1}$], as angular-dispersion measurements show [39].

As an example for a CARS geometry supporting the detection of $A_1(LO)$ phonons, a spectrum taken in $z(xxx, x)\text{-}z$ is shown in Fig. 7(c). Similar to Figs. 7(a) and 7(b), these peaks can be assigned with a tendency to higher anti-Stokes shifts in comparison to SR. Again, the relative scattering intensities of the phonons are comparable to those of SR. However, the CARS intensity of the $A_1(LO_4)$ peak is remarkably high. This is an especially interesting observation because the CARS intensity of $A_1(TO_4)$ was so low that the peak could not be assigned at all. The vibrational motion of the $A_1(LO_4)$ phonon is dominated by a strong vibrational motion of the oxygen atoms within the xy plane [40]. Judging from the atom dislocations alone, it is not obvious why this effect is observed. Here, theoretical calculations are indicated to confirm the strong CARS tendency towards the LO branch of this phonon. Similar to the other two geometries, a peak or group of peaks at ca. $-500\ \mathrm{cm}^{-1}$ is seen. Additionally, a peak at $-745\ \mathrm{cm}^{-1}$ can be detected, which is also visible in the SR spectra of z-cut LN and is assumed to stem from second-order scattering caused by disorder in the crystal structure [41].

As an additional measure to assess the correctness of the predicted selection rules, we analyzed LN in the system geometry $x(zy)\text{-}x$ with a linearly polarized (case 1) and an unpolarized (case 2) broadband Stokes laser. This means that the effective CARS geometry is $x(zzz, y)\text{-}x$ for case 1 and a superposition of $x(zzz, y)\text{-}x$ and $x(zzy, y)\text{-}x$ for case 2. While the selection rules predict the detection of E(TO) phonons in $x(zzy, y)\text{-}x$ (case 2), there are no phonon branches expected for $x(zzz, y)\text{-}x$ (cases 1 and 2). The comparison of the two measurements confirms the validity of the predicted CARS selection rules. The corresponding spectra are provided in the Supplemental Material (Fig. S3) [30].

B. Polarized B-CARS on lithium tantalate

The CARS measurements conducted on LN were repeated on LT to assess the correctness of the selection rules (Fig. 8). Analogously to LN, the corresponding phonons were assigned to the peaks of the PR CARS spectra (Table II). The assignment of the $A_1(TO)$ phonons in $x(zzz, z)\text{-}x$ [Fig. 8(a)] is not as unequivocal as for LN, because various other peaks in the vicinity of the $A_1(TO)$ phonon frequencies are apparent in the spectrum. We can see this effect in the SR spectrum as well, but the PR B-CARS spectrum exhibits distinctly more peaks that are not expected in this geometry.

The $A_1(TO_3)$ peak can be clearly assigned due to its high intensity and isolated spectral position, whereas it can be assumed that the $A_1(TO_1)$ and $A_1(TO_2)$ peaks experience a stronger shift from their spectral position in SR. As for LN,

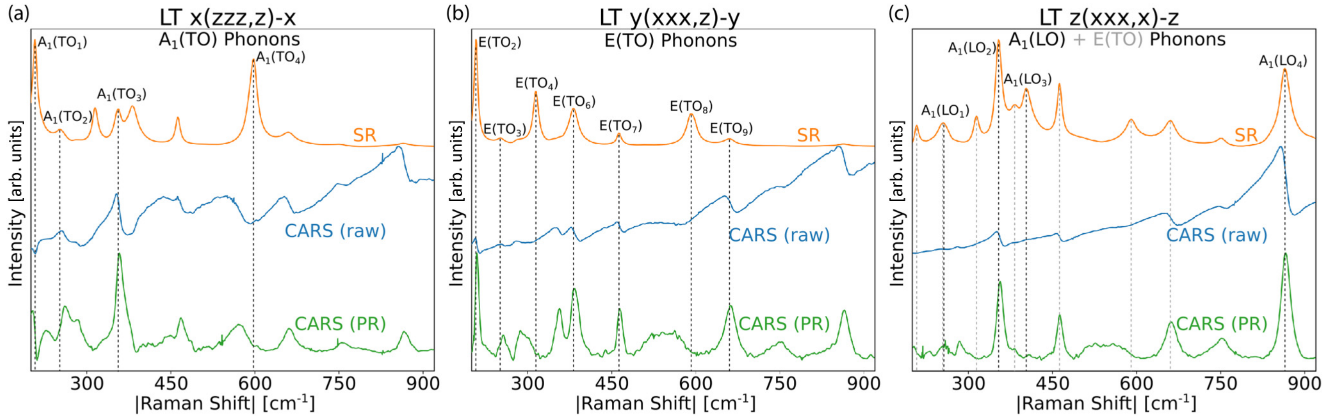

FIG. 8. SR (red), raw CARS (blue) and phase-retrieved CARS spectra (green) of cLT in a) x(zzz,z)-z, b) y(xxx,z)-y and c) z(xxx,x)-z geometry. CARS spectra are plotted over the modulus of the Raman shift for comparison with SR data. The A$_1$(TO), E(TO) and A$_1$(LO) phonons expected for the respective geometry are indicated by dashed lines that refer to reported values of SR phonon frequencies.

the A$_1$(TO$_4$) phonon shows a low CARS efficiency, so that the spectrum does not provide a peak in the expected spectral range. The unassigned peaks in the spectrum belong either to other phonon branches not expected in this geometry or to peaks that cannot be assigned to any one-phonon scattering process, in analogy with the observations in LN. However, these peaks are not as intense relative to the phonon peaks like for the LN spectra, which supports the assumption of a material specific property like an extraordinary NRB signal. Further research is indicated to elucidate whether CARS appears to be more sensitive to possible angular changes on LT than on LN.

A similar behavior can be observed for the E(TO) and A$_1$(LO) phonon peaks in Figs. 8(b) and 8(c). The expected phonon branches in PR B-CARS spectra are in all cases accompanied by additional phonon peaks that are excluded according to the selection rules in the specific geometries. In SR, however, these peaks from parasitic geometries are not detected or only faintly observable. The relative peak intensities of the E(TO) phonons show distinct differences between CARS and SR, e.g., the CARS intensity of E(TO$_9$) is substantially higher than in SR, whereas E(TO$_4$) and E(TO$_8$) exhibit such low CARS intensities that we were not able to determine their peak frequencies in the spectra. The overall observations of the LT investigations confirm the findings of the LN measurements, however, under the caveat that the selection rules are not observed as strictly as in LN. The geometry-dependent CARS measurements and phonon assignments demonstrate that phonon properties are accessible via B-CARS in a similar way as for SR. The predicted selection rules are valid and most of the expected phonons could be assigned to the PR CARS peaks with minor frequency shifts. The relative peak intensities of selected phonons appear to show strong differences to SR. Theoretical modeling is indicated to ascertain the causes for these deviations.

V. CONCLUSIONS AND OUTLOOK

In this case study on cLN and cLT single crystals, we discussed the specific properties of B-CARS measurements on solid-state materials and demonstrated that the phase retrieval of raw CARS spectra allows us to obtain spectral information comparable to standard Raman techniques. Based on phase mismatch calculations, we discussed the nature of signal generation in a collinear backscattering setup. We predicted and experimentally validated CARS selection rules for the C_{3v} point group and unequivocally assigned the majority of CARS peaks in spectra of cLN and cLT. Nevertheless, we observed differences in relative CARS intensity for specific phonon peaks compared with SR and found a group of peaks in all measurements that cannot be caused by single phonon vibrational motions. For future work, theoretical simulations of CARS efficiencies for all detectable phonons and angle-resolved measurements to investigate the sensitivity of CARS for geometry changes are indicated, as well as experiments to quantitatively validate the considerations on phase matching.

These fundamental investigations form the basis for CARS measurements as a high-speed equivalent of SR for the analysis and imaging of solid-state materials or structured surfaces like LN domain walls.

ACKNOWLEDGMENTS

The authors gratefully acknowledge financial support by the Deutsche Forschungsgemeinschaft (DFG) through projects CRC1415 (ID: 417590517), EN 434/41-1 (TOPELEC), INST 269/656-1 FUGG and FOR5044 (ID: 426703838 [42]), as well as the Würzburg-Dresden Cluster of Excellence on “Complexity and Topology in Quantum Matter” - ct.qmat (EXC 2147; ID 39085490).

---

[1] C. L. Evans and X. S. Xie, Coherent anti-Stokes Raman scattering microscopy: Chemical imaging for biology and medicine, Annu. Rev. Anal. Chem. **1**, 883 (2008).

[2] G. I. Petrov, R. Arora, and V. V. Yakovlev, Coherent anti-Stokes Raman scattering imaging of microcalcifications associated with breast cancer, Analyst **146**, 1253 (2021).

[3] C. Zhang, D. Zhang, and J.-X. Cheng, Coherent Raman scattering microscopy in biology and medicine, Annu. Rev. Biomed. Eng. **17**, 415 (2015).

[4] K. Ikeda and K. Uosaki, Coherent phonon dynamics in single-walled carbon nanotubes studied by time-frequency two-dimensional coherent anti-Stokes Raman scattering spectroscopy, Nano Lett. **9**, 1378 (2009).

[5] A. Paddubskaya, D. Rutkauskas, R. Karpicz, G. Dovbeshko, N. Nebogatikova, I. Antonova, and A. Dementjev, Recognition of spatial distribution of CNT and graphene in hybrid structure by mapping with coherent anti-Stokes Raman microscopy, Nanoscale Res. Lett. **15**, 37 (2020).

[6] G. Dovbeshko, O. Fesenko, A. Dementjev, R. Karpicz, V. Fedorov, and O. Y. Posudievsky, Coherent anti-Stokes Raman scattering enhancement of thymine adsorbed on graphene oxide, Nanoscale Res. Lett. **9**, 263 (2014).

[7] J. Koivistoinen, P. Myllyperkio, and M. Pettersson, Time-resolved coherent anti-Stokes Raman scattering of graphene: Dephasing dynamics of optical phonon, J. Phys. Chem. Lett. **8**, 4108 (2017).

[8] A. Virga, C. Ferrante, G. Batignani, D. De Fazio, A. D. G. Nunn, A. C. Ferrari, G. Cerullo, and T. Scopigno, Coherent anti-Stokes Raman spectroscopy of single and multi-layer graphene, Nat. Commun. **10**, 3658 (2019).

[9] J. Ling, X. Miao, Y. Sun, Y. Feng, L. Zhang, Z. Sun, and M. Ji, Vibrational imaging and quantification of two-dimensional hexagonal boron nitride with stimulated Raman scattering, ACS Nano **13**, 14033 (2019).

[10] E. O. Potma, W. P. De Boeij, and D. A. Wiersma, Nonlinear coherent four-wave mixing in optical microscopy, J. Opt. Soc. Am. B **17**, 1678 (2000).

[11] R. P. Davis, A. J. Moad, G. S. Goeken, R. D. Wampler, and G. J. Simpson, Selection rules and symmetry relations for four-wave mixing measurements of uniaxial assemblies, J. Phys. Chem. B **112**, 5834 (2008).

[12] L. Zhou, H. Fu, T. Lv, C. Wang, H. Gao, D. Li, L. Deng, and W. Xiong, Nonlinear optical characterization of 2D materials, Nanomaterials **10**, 2263 (2020).

[13] A. Honardoost, K. Abdelsalam, and S. Fathpour, Rejuvenating a versatile photonic material: Thin-film lithium niobate, Laser Photonics Rev. **14**, 2000088 (2020).

[14] L. Chang, Y. Li, N. Volet, L. Wang, J. Peters, and J. E. Bowers, Thin film wavelength converters for photonic integrated circuits, Optica **3**, 531 (2016).

[15] J. Zhao, C. Ma, M. Rüsing, and S. Mookherjea, High Quality Entangled Photon Pair Generation in Periodically Poled Thin-Film Lithium Niobate Waveguides, Phys. Rev. Lett. **124**, 163603 (2020).

[16] C. Wang, C. Langrock, A. Marandi, M. Jankowski, M. Zhang, B. Desiatov, M. M. Fejer, and M. Lončar, Ultrahigh-efficiency wavelength conversion in nanophotonic periodically poled lithium niobate waveguides, Optica **5**, 1438 (2018).

[17] A. Rao, K. Abdelsalam, T. Sjaardema, A. Honardoost, G. F. Camacho-Gonzalez, and S. Fathpour, Actively-monitored periodic-poling in thin-film lithium niobate photonic waveguides with ultrahigh nonlinear conversion efficiency of 4600% W^{-1} cm^{-2}, Opt. Express **27**, 25920 (2019).

[18] J. Lu, J. B. Surya, X. Liu, A. W. Bruch, Z. Gong, Y. Xu, and H. X. Tang, Periodically poled thin-film lithium niobate microring resonators with a second-harmonic generation efficiency of 250, 000%/W, Optica **6**, 1455 (2019).

[19] J. Zhao, M. Rüsing, U. A. Javid, J. Ling, M. Li, Q. Lin, and S. Mookherjea, Shallow-etched thin-film lithium niobate waveguides for highly-efficient second-harmonic generation, Opt. Express **28**, 19669 (2020).

[20] C. Godau, T. Kämpfe, A. Thiessen, L. M. Eng, and A. Haußmann, Enhancing the domain wall conductivity in lithium niobate single crystals, ACS Nano **11**, 4816 (2017).

[21] T. Kämpfe, B. Wang, A. Haußmann, L.-Q. Chen, and L. M. Eng, Tunable non-volatile memory by conductive ferroelectric domain walls in lithium niobate thin films, Crystals **10**, 804 (2020).

[22] C. H. Camp, Y. J. Lee, and M. T. Cicerone, Quantitative, comparable coherent anti-Stokes Raman scattering (CARS) spectroscopy: Correcting errors in phase retrieval, J. Raman Spectrosc. **47**, 408 (2016).

[23] H. Lotem, R. T. Lynch Jr, and N. Bloembergen, Interference between Raman resonances in four-wave difference mixing, Phys. Rev. A **14**, 1748 (1976).

[24] J.-X. Cheng, A. Volkmer, and X. S. Xie, Theoretical and experimental characterization of coherent anti-Stokes Raman scattering microscopy, J. Opt. Soc. Am. B **19**, 1363 (2002).

[25] J.-X. Cheng and X. S. Xie, Coherent anti-Stokes Raman scattering microscopy: Instrumentation, theory, and applications, J. Phys. Chem. B **108**, 827 (2004).

[26] W. M. Tolles, J. Nibler, J. McDonald, and A. Harvey, A review of the theory and application of coherent anti-Stokes Raman spectroscopy (CARS), Appl. Spectrosc. **31**, 253 (1977).

[27] E. M. Vartiainen, Phase retrieval approach for coherent anti-Stokes Raman scattering spectrum analysis, J. Opt. Soc. Am. B **9**, 1209 (1992).

[28] A. Bohlin, B. D. Patterson, and C. J. Kliewer, Communication: Simplified two-beam rotational CARS signal generation demonstrated in 1D, J. Chem. Phys. **138**, 081102 (2013).

[29] M. Rüsing, J. Zhao, and S. Mookherjea, Second harmonic microscopy of poled *x*-cut thin film lithium niobate: Understanding the contrast mechanism, J. Appl. Phys. **126**, 114105 (2019).

[30] See Supplemental Material at http://link.aps.org/supplemental/10.1103/PhysRevB.104.224308 for details about the measurement setup and phase retrieval, the CARS selection rules of C_{3v} crystals, and additional spectra of LN and LT.

[31] S. Margueron, A. Bartasyte, A. M. Glazer, E. Simon, J. Hlinka, I. Gregora, and J. Gleize, Resolved E-symmetry zone-centre phonons in $LiTaO_3$ and $LiNbO_3$, J. Appl. Phys. **111**, 104105 (2012).

[32] D. Tuschel, The effect of microscope objectives on the Raman spectra of crystals, Spectroscopy **32**, 14 (2017).

[33] M. Rüsing, S. Sanna, S. Neufeld, G. Berth, W. G. Schmidt, A. Zrenner, H. Yu, Y. Wang, and H. Zhang, Vibrational properties of $LiNb_{1-x}Ta_xO_3$ mixed crystals, Phys. Rev. B **93**, 184305 (2016).

[34] S. Sanna, S. Neufeld, M. Rüsing, G. Berth, A. Zrenner, and W. G. Schmidt, Raman scattering efficiency in $LiTaO_3$ and $LiNbO_3$ crystals, Phys. Rev. B **91**, 224302 (2015).

[35] A. Bartasyte, S. Margueron, A. M. Glazer, E. Simon, I. Gregora, S. Huband, and P. A. Thomas, Vibrational modes and overlap matrix of $LiNb_{1-x}Ta_xO_3$ mixed crystals, Phys. Rev. B **99**, 094306 (2019).

[36] K. Parlinski, Z. Q. Li, and Y. Kawazoe, Ab initio calculations of phonons in $LiNbO_3$, Phys. Rev. B **61**, 272 (2000).

[37] M. Friedrich, A. Riefer, S. Sanna, W. G. Schmidt, and A. Schindlmayr, Phonon dispersion and zero-point renormalization of $LiNbO_3$ from density-functional perturbation theory, J. Phys.: Condens. Matter **27**, 385402 (2015).

[38] M. Friedrich, A. Schindlmayr, W. G. Schmidt, and S. Sanna, $LiTaO_3$ phonon dispersion and ferroelectric transition calculated from first principles, Phys. Status Solidi B **253**, 683 (2016).

[39] X. Yang, G. Lan, B. Li, and H. Wang, Raman spectra and directional dispersion in $LiNbO_3$ and $LiTaO_3$, Phys. Status Solidi B **142**, 287 (1987).

[40] V. Caciuc, A. V. Postnikov, and G. Borstel, Ab initio structure and zone-center phonons in $LiNbO_3$, Phys. Rev. B **61**, 8806 (2000).

[41] M. D. Fontana and P. Bourson, Microstructure and defects probed by Raman spectroscopy in lithium niobate crystals and devices, Appl. Phys. Rev. **2**, 040602 (2015).

[42] http://www.For5044.de.